



Evolution of Magnetic Reconnection in an Electron-scale Current Sheet

Yundan Guan¹ , Quanming Lu^{1,2,3} , San Lu^{1,2,3} , and Rongsheng Wang^{1,2,3} ¹ CAS Center for Excellence in Comparative Planetology, CAS Key Lab of Geospace Environment, School of Earth and Space Sciences, University of Science and Technology of China, Hefei, Anhui, People's Republic of China; qmlu@ustc.edu.cn, lusan@ustc.edu.cn² Deep Space Exploration Laboratory, Hefei, Anhui, People's Republic of China³ Collaborative Innovation Center of Astronautical Science and Technology, Harbin, People's Republic of China
Received 2024 October 17; revised 2024 November 20; accepted 2024 December 03; published 2025 January 20

Abstract

Recently, a new type of magnetic reconnection, electron-only reconnection—where there is no obvious ion flow and heating—has been observed in various plasma environments. Previous kinetic simulations have shown that electron-only reconnection is a precursor of standard reconnection. In this paper, by performing a 2.5-dimensional particle-in-cell simulation, we investigate the evolution of electron-only magnetic reconnection to standard magnetic reconnection in a current sheet, whose initial width is of the electron inertial length. In the electron-only reconnection stage, electron outflow produces the electron-scale B_z pileup, and ions are slightly accelerated in the outflow direction by the Hall electric field force. As the reconnection electric field expands and B_z is piled up to the ion scale, ions start to be further accelerated inside the ion diffusion region and reflected by the B_z to the outflow direction. With B_z pileup as the bond, ions gradually transit from being accelerated by the Hall electric field to being coupled in reconnection by the Lorentz force.

Unified Astronomy Thesaurus concepts: Plasma physics (2089); Space plasmas (1544); Planetary magnetospheres (997)

1. Introduction

Magnetic reconnection, accompanied by the topological change in magnetic field lines, provides a physical mechanism for transferring magnetic energy into plasma kinetic energy (D. Biskamp, 2000; J. Birn & E. R. Priest 2007; M. Yamada et al. 2010; S. Wang & Q. M. Lu 2019; M. Hesse & P. A. Cassak 2020). Magnetic reconnection has been observed ubiquitously in various plasma environments, including the solar atmosphere (C. J. Nelson et al. 2013; C. Shen et al. 2022; C. Hou et al. 2024; Zhuo et al. 2024), interplanetary space (T. D. Phan et al. 2006; Z. Vörös et al. 2021; R. S. Wang et al. 2023), Earth's and planetary magnetospheres (T. L. Zhang et al. 2012; Q. M. Lu et al. 2022; S. M. Wang et al. 2024), and laboratory plasma (H. Ji et al. 2022). It is widely believed that magnetic reconnection is responsible for explosive phenomena throughout the Universe, such as solar flares, coronal mass ejections, and Earth's magnetospheric storms and substorms (S. Masuda et al. 1994; J. Lin & T. G. Forbes 2000; V. Angelopoulos et al. 2008; J. L. Burch et al. 2016; R. B. Torbert et al. 2018). In standard magnetic reconnection, the diffusion region has a multiscale structure, where an electron-scale electron diffusion region (EDR) is embedded in an ion-scale ion diffusion region (IDR; J. Birn et al. 2001; J. Birn & M. Hesse 2001; T. Nagai et al. 2001; P. L. Pritchett, 2001; M. A. Shay et al. 2001; A. L. Borg et al. 2005; Q. M. Lu et al. 2010; J. L. Burch et al. 2016).

Recently, a new type of reconnection—electron-only reconnection has been observed in Earth's magnetosheath (T. D. Phan et al. 2018; J. E. Stawarz et al. 2019, 2022), the transition region of the bow shock (I. Gingell et al. 2020; N. Bessho et al. 2022), magnetopause boundary layer (S. Huang et al. 2021), magnetotail (R. S. Wang et al. 2018, 2020; H. Y. Man et al. 2020;

M. Hubbert et al. 2021, 2022), and laboratory plasmas (J. Ng et al. 2022; P. Y. Shi et al. 2022a, 2022b; L. Sang et al. 2022). Electron-only reconnection usually occurs in an electron current sheet, where the current is carried mostly by electrons, and the width is on the order of the electron inertial length. Unlike standard reconnection, electron-only reconnection has no obvious ion heating and flow, but super-Alfvénic electron outflow and electron heating can still be observed. (T. D. Phan et al. 2018; R. S. Wang et al. 2018, 2020; P. S. Pyakurel et al. 2019; S. Lu et al. 2020b, 2022; Y. Guan et al. 2023).

Kinetic simulations have demonstrated that electron-only reconnection occurs when the size of the simulation domain is smaller or comparable to the ion gyroradius, and it does not evolve into standard reconnection because the reconnection region is too small for the ions to be coupled with the magnetic structures (P. S. Pyakurel et al. 2019; Y. Guan et al. 2023). Such kind of electron-only reconnection may result in coherent structures formed in a turbulent plasma (F. Califano et al. 2020; C. Vega et al. 2020; Q. M. Lu et al. 2021, 2024; J. Ng et al. 2022). When the simulation domain is much larger than the ion inertial length, electron-only reconnection may also occur in an electron-scale current sheet, which evolves from an ion-scale current sheet by an external driver (P. L. Pritchett & F. V. Coroniti 1994). Such kind of electron-only reconnection is considered a transition phase toward standard reconnection, and it eventually evolves into standard reconnection (S. Lu et al. 2020b, 2022; Wang et al. 2020; M. Hubbert et al. 2021, 2022).

However, whether electron-only reconnection is an essential precursor to standard reconnection is still unknown. It is also unknown how ions become coupled in the transition from electron-only to standard reconnection. In this paper, by performing a 2.5-dimensional particle-in-cell (PIC) simulation, an electron-dominated current sheet is given. The width of the current sheet is on the order of the electron inertial length, while the simulation domain is sufficiently large to accommodate standard magnetic reconnection. The process of

magnetic reconnection experiences two stages, it first enters the stage of electron-only reconnection and then evolves into the stage of standard reconnection. The pileup of the magnetic field in the outflow region. We further show that with B_z pileup as the bond, ions gradually become coupled in reconnection by the Lorentz force.

2. Simulation Model

In this paper, a PIC simulation model is used, which has been successfully applied to study magnetic reconnection (X. R. Fu et al. 2006; C. Huang et al. 2010, 2015; Q. M. Lu et al. 2010; C. Chang et al. 2021). The simulation is 2.5-dimensional, i.e., the simulation domain is two-dimensional and the particle velocity is three-dimensional. The simulation is performed in the x - z plane. The magnetic field is normalized by the magnitude of the upstream magnetic field B_0 , density to the maximum of the current sheet density n_0 , time to Ω_i^{-1} (where $\Omega_i = eB_0/m_i$ is the ion gyrofrequency), lengths to the ion inertial length $d_i = m_i/(\mu_0 n_0 e^2)$, velocities to the Alfvén speed $V_A = B_0/\sqrt{\mu_0 m_i n_0}$, electric fields to $E_0 = B_0 V_A$, and temperatures to $m_i V_A^2$.

The current sheet setup refers to the real Earth's magnetotail environment, that is, the ion temperature T_i is several times higher than the electron temperature T_e (A. V. Artemyev et al. 2011); a thin and strong electron current sheet embedded in a thick and weak ion current sheet (Y. Asano et al. 2003; A. V. Artemyev et al. 2009); the normal electric field E_n (or E_z) point toward the center of the current sheet (S. Lu et al. 2019; Z. Zhang et al. 2024). Thus, the charged, electron-dominant current sheet configuration is used (S. Lu et al. 2020a). The initial ion temperature is $T_i = 0.45 m_i V_A^2$, and the initial electron temperature is $T_e = 0.05 m_i V_A^2$. The initial drift velocity ratio of ions and electrons V_i/V_e is 1/9. The ion-to-electron mass ratio $m_i/m_e = 1836$ is used, and the initial half-width of the current sheets δ is $0.06 d_i \approx 2.6 d_e$. The upstream background density is $n_b = 0.1 n_0$. Figure 1 shows the profiles of the initial magnetic field, current sheet, number density, and electric field.

The grid size is $dx = dz = 0.005 d_i$, and the grid number is $N_x = N_z = 1200$. Therefore, the size of the simulation domain is $L_x = L_z = L = 6 d_i$. The time step is $dt = 10^{-5} \Omega_i^{-1}$. The speed of light is $c = 50 V_A$. We use 1000 particles (per species) per cell to represent n_0 in the simulation. Periodic boundary conditions are used in the x -direction. Perfect conducting boundary conditions for electromagnetic fields and reflecting boundary conditions for particles are used in the z -direction. No initial perturbation is added to the initial magnetic flux, and no external driver is added to the boundary.

3. Simulation Results

In this case, there are five x -lines spontaneously triggered within the current sheet, and we focus on the x -line with an entire evolution process. Figure 2 shows the time history of the reconnection rate and the ion temperature at the reconnection site. Depending on whether the ion temperature starts to increase, this reconnection can be divided into two stages: the period $t < 1 \Omega_i^{-1}$ is the first stage (Stage I) when reconnection has been triggered but the ion temperature at the reconnection site has not increased; the period $t > 1 \Omega_i^{-1}$ is the second stage (Stage II) when the ion temperature at the reconnection site starts to increase. In Stage I, the reconnection rate reaches the

maximum of 0.33 at $t = 0.24 \Omega_i^{-1}$, and in Stage II, the reconnection rate reaches the maximum of 0.20 at $t = 5.07 \Omega_i^{-1}$.

Figure 3 shows ion and electron bulk velocity in the x -direction and the increment of ion and electron temperature in the whole simulation domain. As mentioned above, in Figure 3(a) at $t = 0.24 \Omega_i^{-1}$, there are five pairs of electron super-Alfvénic bidirectional jets generated by five x -lines, respectively, and the x -line we focused on is situated at the center of the simulation domain. At this time the x -line region is roughly boxed in orange ($x, z \in [-0.3 d_i, 0.3 d_i]$), and in this region, the ion outflow speed is no more than $0.1 V_A$, as shown in Figure 3(b). Compared to the initial temperature, the electron temperature increases by about $0.01 m_i V_A^2$ at the reconnection site, and the ions are not heated, as shown in Figures 3(c) and (d). Therefore, the Stage I is electron-only reconnection. When this reconnection goes through about one ion cyclotron time, in Figures 3(e) and (f), besides the electron super-Alfvénic outflow, the ion outflow exceeding $0.1 V_A$ is generated. The x -line region at $t = 1.00 \Omega_i^{-1}$ is roughly boxed in green ($x, z \in [-1.5 d_i, 1.5 d_i]$). In Figures 3(g) and (h), heated electrons and ions can be seen inside the magnetic islands in the outflow region. The ion outflow $V_{ix} > 0.1 V_A$ indicates that reconnection is evolving from the electron-only reconnection stage to the standard reconnection stage. Then reconnection continues to evolve. In Figures 3(i) and (j), the electron outflow reaches $3.9 V_A$ and the ion outflow reaches $0.4 V_A$ at $t = 5.07 \Omega_i^{-1}$. The x -line region at $t = 5.07 \Omega_i^{-1}$ is roughly boxed in purple ($x, z \in [-2.5 d_i, 2.5 d_i]$). In Figures 3(k) and (l), heated electrons and ions are inside the diffusion region and the outflow region, respectively. The ion and electron acceleration and heating demonstrate that this reconnection eventually evolves into the stage of standard reconnection.

To study how the ions respond to reconnection at different stages, we consider the x -component of the ion momentum equation:

$$m_i \frac{dV_{ix}}{dt} = eE_x + e(\mathbf{V}_i \times \mathbf{B})_x - (\nabla \cdot \tilde{\mathbf{P}}_i)_x / n_i. \quad (1)$$

The terms on the right side of Equation (1) are the electric field force term, the Lorentz force term, and the ion pressure gradient force term, respectively. Figure 4 shows the profiles of the three force terms along $z = 0$. During the whole reconnection, the electric field force term and the Lorentz force term accelerate the ion outflow, while the ion pressure gradient force term decelerates the ion outflow. The electric field force term represents the effect of the Hall electric field; the Lorentz force term $e(\mathbf{V}_i \times \mathbf{B})_x \approx eV_{iy} B_z$ represents the process in which ions are accelerated inside the IDR and then are reflected by the B_z pileup to the x -direction. In Stage I (Figure 4(a)), the Lorentz force is weak, meaning the impact of the reconnection field on ions is weak. Although ions seem not to respond to the reconnection electric field, they are still accelerated by the Hall electric field, which is formed by the charge separation caused by the rapidly ejected electron outflow. During the transition (Figure 4(b)), the Lorentz force starts to increase, becoming closer to the electric field force, which represents the ions starting to be accelerated by the reconnection electric field. In Stage II (Figure 4(c)), the Lorentz force and the electric field force work together against the pressure gradient force, eventually accelerating the ion outflow to $0.4 V_A$.

Figure 5 shows the evolution of the reconnection electric field E_y , ion frozen-in criterion $(\mathbf{E} + \mathbf{V}_i \times \mathbf{B})_y$, and electron frozen-in

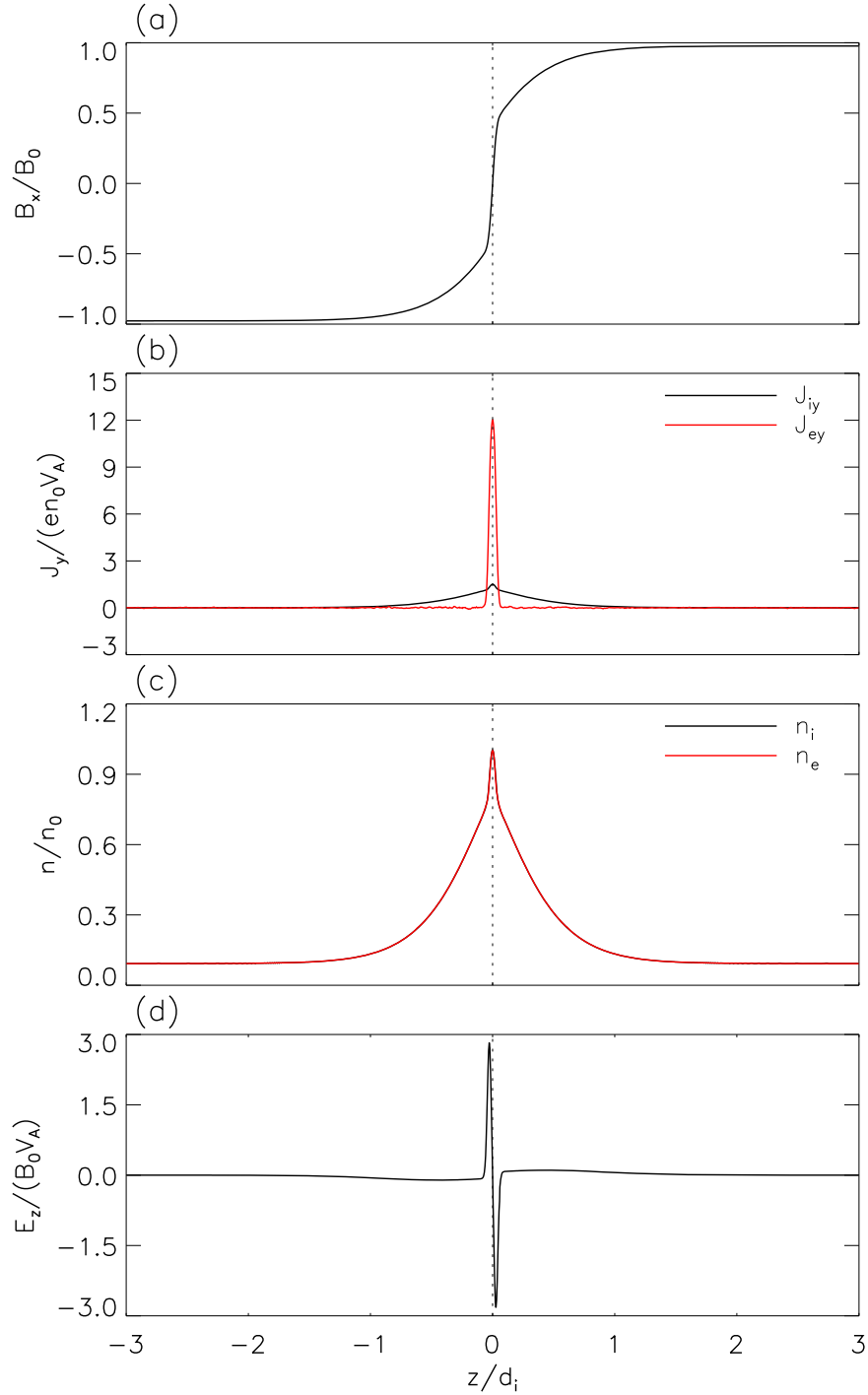


Figure 1. Profiles of (a) magnetic field B_x , (b) current density J_y , J_{ey} , (c) number density n_i , n_e , and (d) electric field E_z across the current sheet as a function of z for the charged, electron-dominant current sheet in this case.

criterion $(\mathbf{E} + \mathbf{V}_e \times \mathbf{B})_y$. In Figure 5(a), at $t = 0.24\Omega_i^{-1}$ in Stage I, the reconnection electric field E_y is of sub-ion scale, whose half-length is about $0.2d_i$. The electron frozen-in criterion $(\mathbf{E} + \mathbf{V}_e \times \mathbf{B})_y$ characterizes the multiscale structure of the EDR: the inner EDR where the $(\mathbf{E} + \mathbf{V}_e \times \mathbf{B})_y > 0$ and the outer EDR $(\mathbf{E} + \mathbf{V}_e \times \mathbf{B})_y < 0$ (H. Karimabadi et al. 2007; M. A. Shay et al. 2007). The half-length of the inner EDR at this stage is about $3.4d_e$. It is worth noting that the ion frozen-in criterion $(\mathbf{E} + \mathbf{V}_i \times \mathbf{B})_y$ almost equals E_y at this time, which indicates that although the reconnection electric field breaks the ion frozen-in condition on its scale, a fast ion outflow is not

generated (consistent with Figure 3(b)), so $(\mathbf{V}_i \times \mathbf{B})_y \approx 0$. Only the ion frozen-in criterion is broken but the acceleration effect of the reconnected electric field represented by the Lorentz force is weak (Figure 4(a)), it seems that the IDR is not formed in Stage I. Figure 5(b) shows the transition from the electron-only reconnection stage to the standard reconnection stage. The reconnection field extends to a half-length of $0.8d_i$ and the electron-scale inner EDR still exists, whose half-length is about $4.7d_e$ at this time. However, $(\mathbf{E} + \mathbf{V}_i \times \mathbf{B})_y$ no longer exactly equals E_y , which means ion outflow exceeding $0.1V_A$ starts to form (consistent with Figure 3(f)). At this time the acceleration

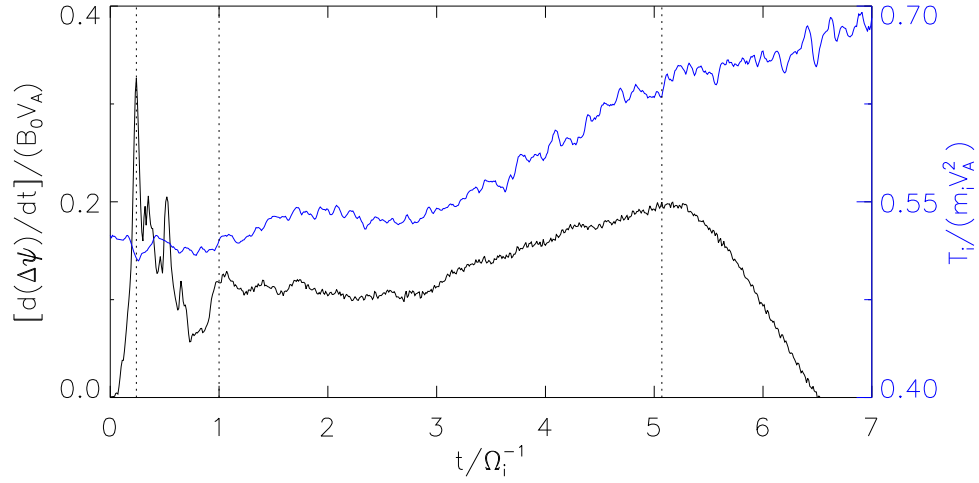


Figure 2. Time history of the reconnection rate (black solid line) and the ion temperature (blue solid line). $t = 0.24$, $t = 1.00\Omega_i^{-1}$, and $t = 5.07\Omega_i^{-1}$ are presented by the black dashed lines. The reconnection rate is calculated by the time derivative of the magnetic flux between the x-point and the o-point. The ion temperature is calculated by $T_i = (1/3)(P_{ixx} + P_{yy} + P_{zz})/n_i$ at the reconnection site.

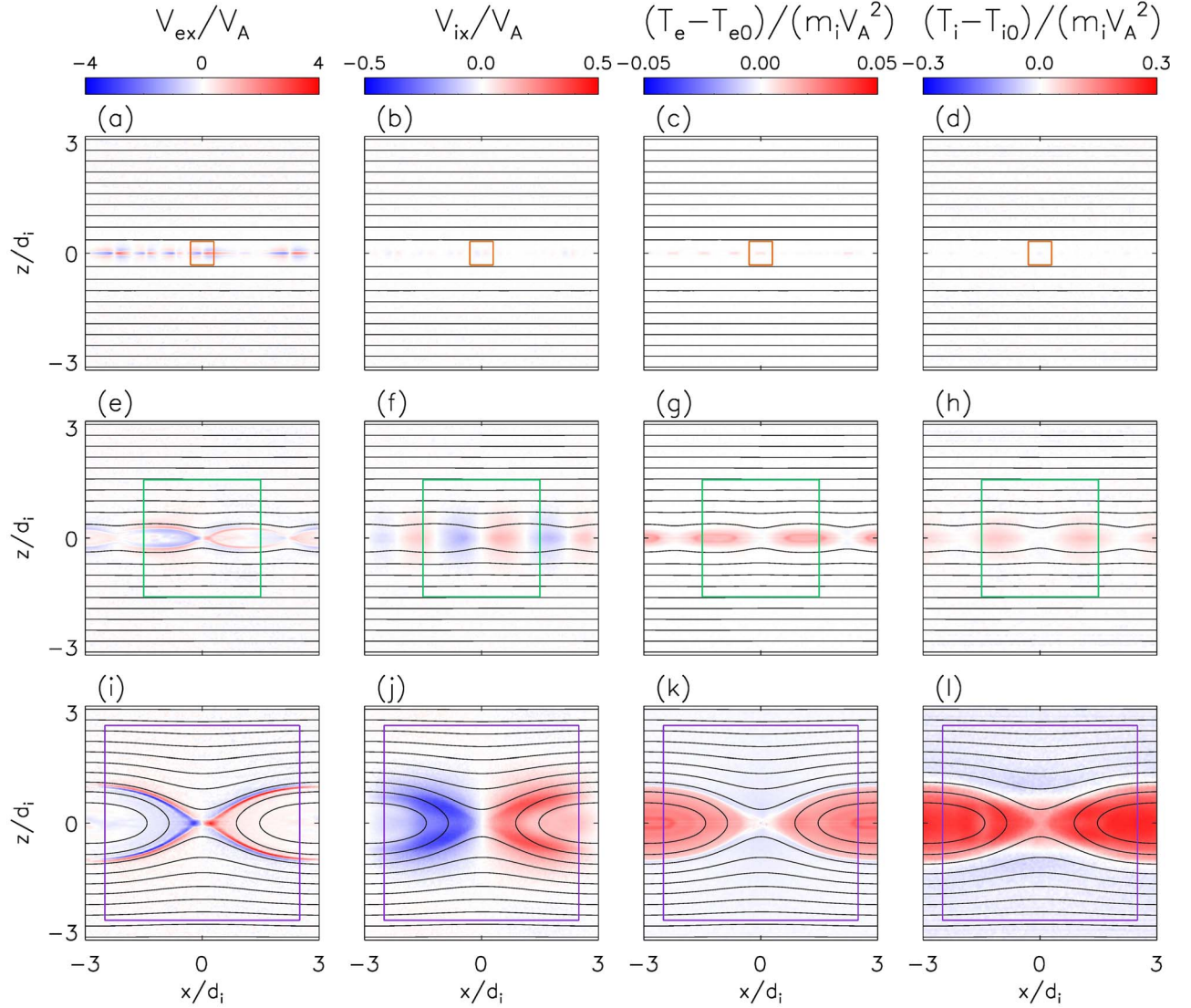


Figure 3. Overview of the case in the full simulation domain at $t =$ (a)–(d) $0.24\Omega_i^{-1}$, (e)–(h) $1.00\Omega_i^{-1}$, and (i)–(l) $5.07\Omega_i^{-1}$. (a), (e), and (i): the electron bulk velocity in the x -direction. (b), (f), and (j): the ion bulk velocity in the x -direction. (c), (g), and (k): the increment of electron temperature. (d), (h), and (l): the increment of ion temperature.

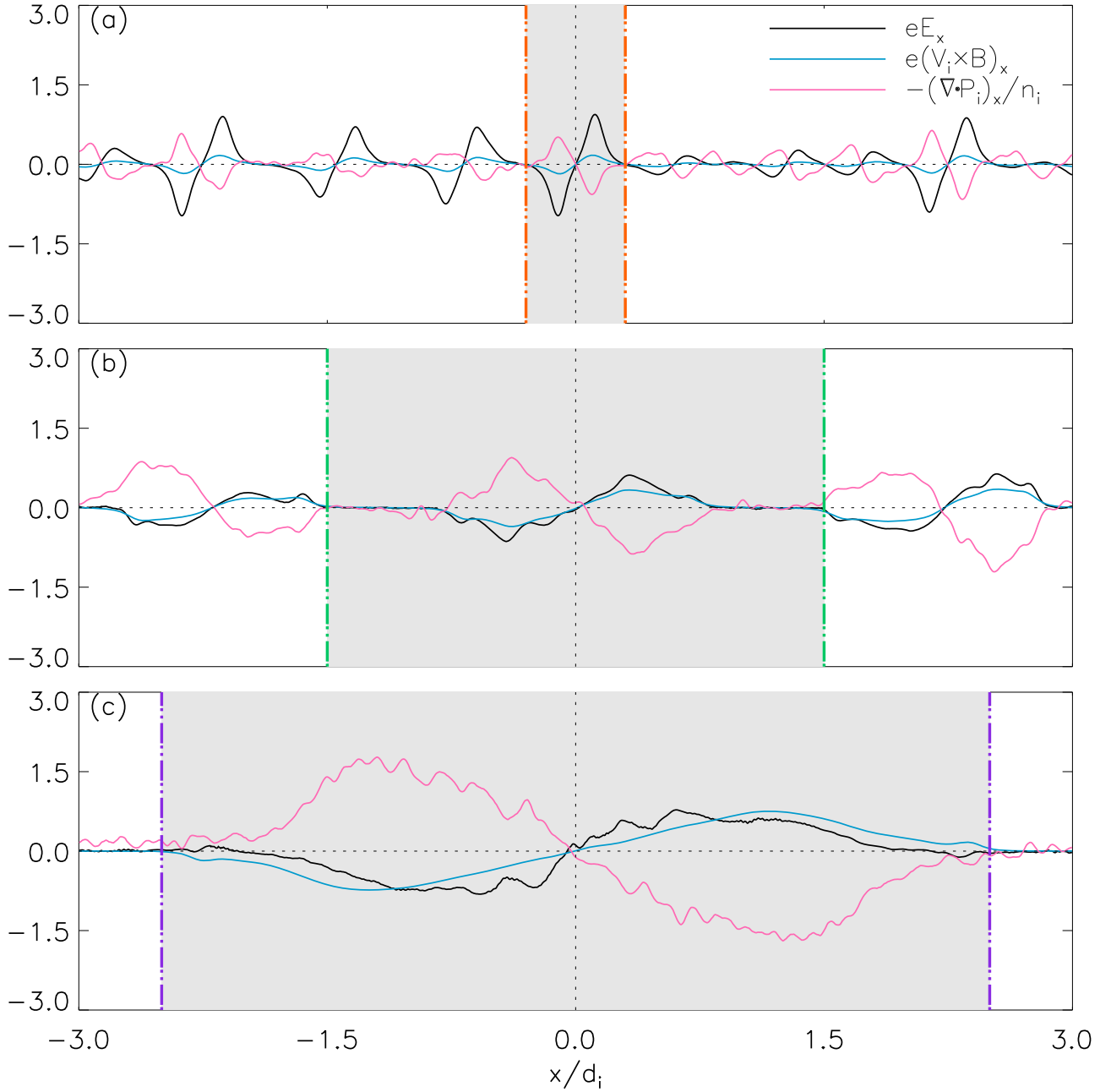


Figure 4. The force terms on the right side of the ion momentum equation in the x -direction at $t =$ (a) $0.24\Omega_i^{-1}$, (b) $1.00\Omega_i^{-1}$, and (c) $5.07\Omega_i^{-1}$. The profiles of the electric field force term eE_x (black line), the Lorentz force term $e(\mathbf{V}_i \times \mathbf{B})_x$ (blue line), and the ion pressure gradient force term $-(\nabla \cdot \mathbf{P}_i)_x/n_i$ (pink line) are taken along $z = 0$. The shadow regions delineated by the orange, green, and purple dashed-dotted lines correspond to the same color boxes in Figure 3.

of the reconnection electric field on ions also becomes nonnegligible (Figure 4(b)), meaning the IDR starts to form. After entering Stage II, as shown in Figure 5(c), the reconnection electric field extends to nearly the whole simulation domain. Both the EDR with a half-length of $6.8d_e$ and the IDR with a half-length of $1.8d_i$ are formed.

Figure 6 shows a further analysis of the B_z pileup. In Stage I (Figure 6(a)), only electron high-speed bidirectional outflows are formed, and the magnetic field B_z is piled just outside the inner EDR. As reconnection continues, the reconnection electric field expands and the B_z keeps piling up. As the reconnection electric field expands to the ion scale, the B_z pileup becomes large enough to reflect the ions that are accelerated by the reconnection electric field to the x -direction,

and then the ion outflow at the same scale as the B_z pileup appears (Figure 6(b)). In Stage II (Figure 6(c)), both electrons and ions are accelerated in their diffusion regions, respectively, and are reflected by the B_z . Ion and electron outflow in turn build up the B_z , resulting in the ion-scale B_z pileup.

The first column in Figure 7 shows the Hall quadrupole magnetic field. As the B_z continues to pile up, the opening angle of the separatrices gradually increases. In magnetic reconnection, due to the electron inflow along the magnetic lines just outside the separatrices and the electron outflow along the magnetic lines just inside the separatrices, an in-plane electron current system is formed (T. Nagai et al. 2003). In the process of increasing the separatrix opening angle, the electron current system also broadens in the z -direction. Thus,

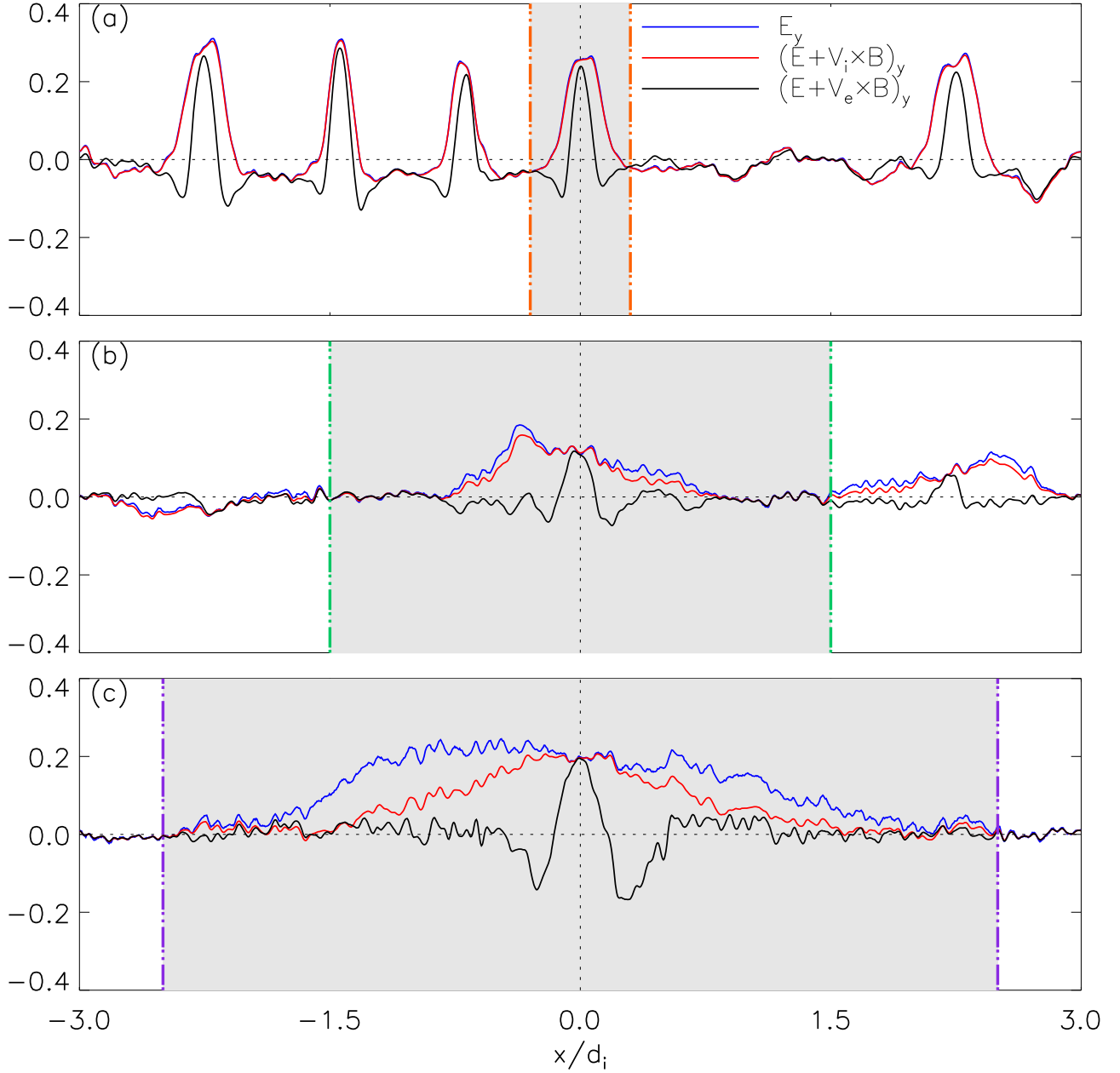


Figure 5. The reconnection electric field E_y , the electron frozen-in criterion $(\mathbf{E} + \mathbf{V}_e \times \mathbf{B})_y$, and the ion frozen-in criterion $(\mathbf{E} + \mathbf{V}_i \times \mathbf{B})_y$ at $t =$ (a) $0.24\Omega_i^{-1}$, (b) $1.00\Omega_i^{-1}$, and (c) $5.07\Omega_i^{-1}$. The profiles of E_y (blue line), $(\mathbf{E} + \mathbf{V}_e \times \mathbf{B})_y$ (red line), and $(\mathbf{E} + \mathbf{V}_i \times \mathbf{B})_y$ (black line) are taken along $z = 0$. The shadow regions delineated by the orange, green, and purple dashed-dotted lines correspond to the same color boxes in Figure 3.

the out-of-plane Hall quadrupole magnetic field B_y , generated by this electron current system (Q. M. Lu et al. 2010; S. Lu et al. 2011) extends in the z -direction, as shown in Figures 7(a), (d), and (g).

The second and third columns in Figure 7 show the in-plane electric field during this reconnection. In the collisionless reconnection, when the electrons and ions are demagnetized at different scales, the in-plane Hall electric field is generated due to the charge separation (J. R. Wygant et al. 2005; M. V. Goldman et al. 2016; S. Lu et al. 2021). In Figures 7(b) and 6(c), in Stage I, due to the lack of the ion-scale outflow, the scale of the in-plane Hall electric field is confined to the electron scale. (In fact, E_z at this time consists of the z -component of the Hall electric field and the initial electric field that has not fully decayed, but it can be

confirmed that both fields are on the electron scale.) In Figures 7(e) and (f), in the transition from the electron-only reconnection stage to the standard reconnection stage, ion-scale outflow increases rapidly, and the Hall electric field expands. Eventually, as ions are sufficiently coupled in reconnection, the Hall electric field extends to the ion scale, as shown in Figures 7(h) and (i).

Figure 8(a) shows the out-of-plane current sheet in Stage I, and Figures 8(b)–(f) show the profiles along the dashed trajectory. The scales of the Hall magnetic field B_y , the B_z pileup, the Hall electric field E_x, E_z , and the electron outflow V_{ex} are confined to the electron current sheet. Meanwhile, in Stage II shown in Figures 8(g)–(l), the scales of the above reconnection signatures not only exist inside the electron current sheet but extend to several ion inertial lengths.

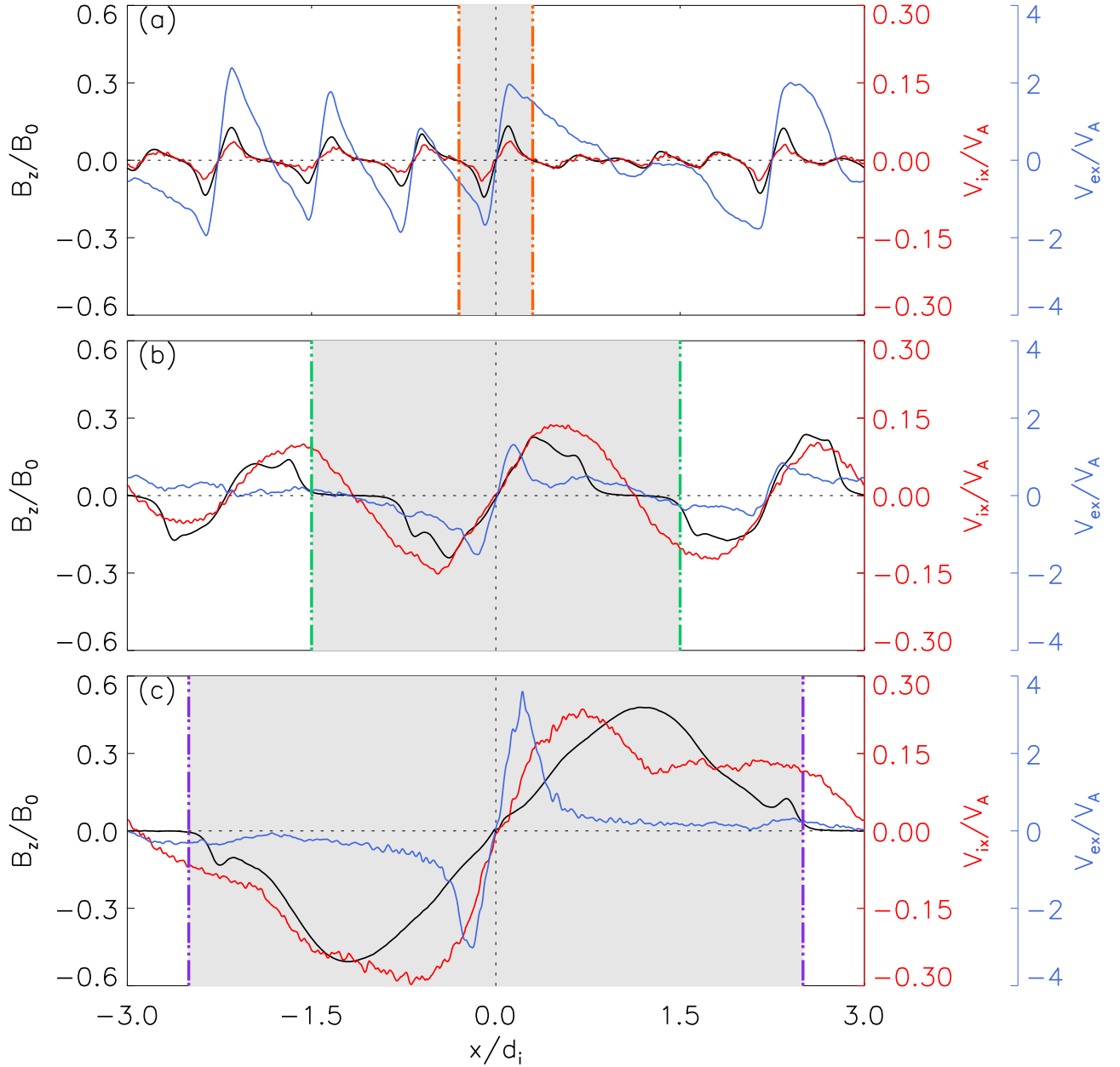


Figure 6. The profiles of B_z pileup (black line), ion bulk velocity in the x -direction V_{ix} (red line), and electron bulk velocity in the x -direction V_{ex} (blue line) along $z = 0$ at $t =$ (a) $0.24\Omega_i^{-1}$, (b) $1.00\Omega_i^{-1}$, and (c) $5.07\Omega_i^{-1}$. The shadow regions delineated by the orange, green, and purple dashed-dotted lines correspond to the same color boxes in Figure 3.

Figure 9 shows the energy budgets in the electron-only reconnection stage at $t = 0.24\Omega_i^{-1}$. To describe the magnetic field energy conversion, the field energy conversion equation

$$\frac{\partial w_B}{\partial t} + \frac{\partial w_E}{\partial t} + \nabla \cdot \mathbf{S} = -\mathbf{J} \cdot \mathbf{E} \quad (2)$$

is considered. Because the electric field energy density w_E is small and negligible, the equation becomes the magnetic energy conversion equation

$$\frac{\partial w_B}{\partial t} + \nabla \cdot \mathbf{S} = -\mathbf{J} \cdot \mathbf{E}, \quad (3)$$

where $w_B = B^2/(2\mu_0)$ is the magnetic energy density, $\mathbf{S} = \mathbf{E} \times \mathbf{B}/\mu_0$ is the Poynting vector, $\mathbf{J} = \mathbf{J}_i + \mathbf{J}_e$ is the total current density, and \mathbf{E} is the electric field. The results of $\frac{\partial w_B}{\partial t}$,

$\nabla \cdot \mathbf{S}$ and $\frac{\partial w_B}{\partial t} + \nabla \cdot \mathbf{S}$ are shown in Figures 9(a)–(c). The results show that the energy source at the electron-only reconnection site is mainly the inflowing Poynting flux, and such energy is converted to the electrons and ions through $\mathbf{J} \cdot \mathbf{E}$. Figure 9(d) shows the work done by the electric field $\mathbf{J} \cdot \mathbf{E}$. The work done by the electric field $\mathbf{J} \cdot \mathbf{E}$ can be divided into two parts, the work done to ions $\mathbf{J}_i \cdot \mathbf{E}$ (Figure 9(e)) and the work done to electrons $\mathbf{J}_e \cdot \mathbf{E}$ (Figure 9(f)). We delineate the region where $\mathbf{J} \cdot \mathbf{E}$ is strong using a green box and integrate $\mathbf{J}_i \cdot \mathbf{E}$ and $\mathbf{J}_e \cdot \mathbf{E}$ in this region, respectively. $\iint \mathbf{J}_e \cdot \mathbf{E} \, dx dy / \iint \mathbf{J} \cdot \mathbf{E} \, dx dy$ equals 66.3%, showing that the incoming Poynting flux gives the energy mostly to the electrons.

The electron and ion kinetic energy density at $t = 0.24\Omega_i^{-1}$ are also calculated, as shown in Figure 10. The green box

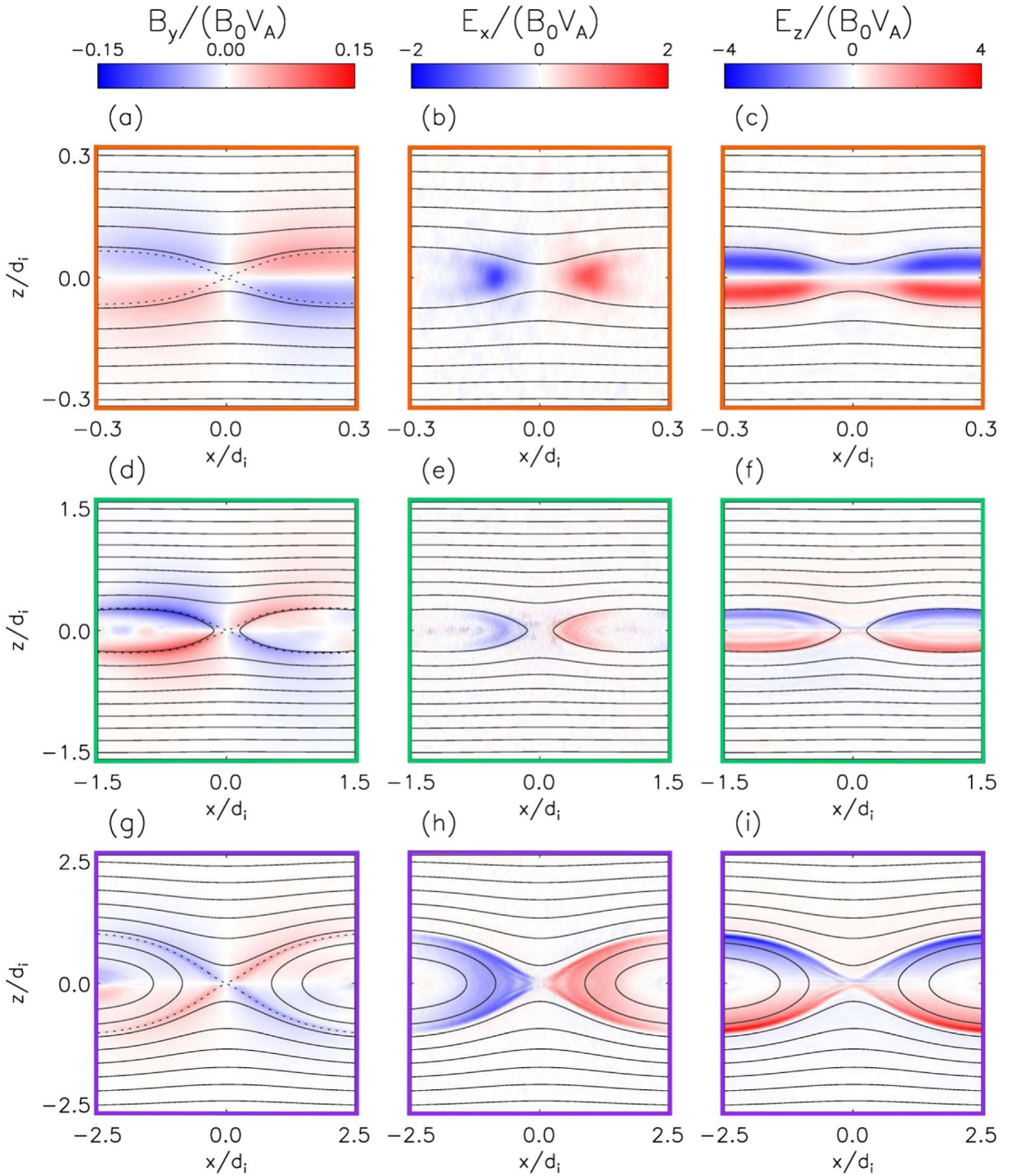


Figure 7. The Hall magnetic field B_y , and the in-plane electric field E_x and E_z at $t =$ (a)–(c) $0.24\Omega_i^{-1}$, (d)–(f) $1.00\Omega_i^{-1}$, and (g)–(i) $5.07\Omega_i^{-1}$. The orange, green, and purple boxes in Figure 6 correspond to the same color boxes in Figure 3.

delineates the outflow region, and the kinetic energy densities are integrated within the green box. The result is that the ion kinetic energy is about 63% of the electron kinetic energy.

4. Conclusions and Discussion

In this paper, with a 2.5-dimensional PIC simulation model, we study reconnection spontaneously triggered inside the electron-dominant current sheet with ion-scale length. This

reconnection first enters the electron-only reconnection stage and then evolves into the standard reconnection stage. In the electron-only reconnection stage, electron outflow produces the electron-scale B_z pileup, and ions are accelerated in the outflow direction by the Hall electric field force. As the reconnection electric field expands and B_z is piled up to the ion scale, ions start to be accelerated inside the IDR and reflected by the B_z to the outflow direction. With B_z pileup as the bond, ions gradually transit from being accelerated by the

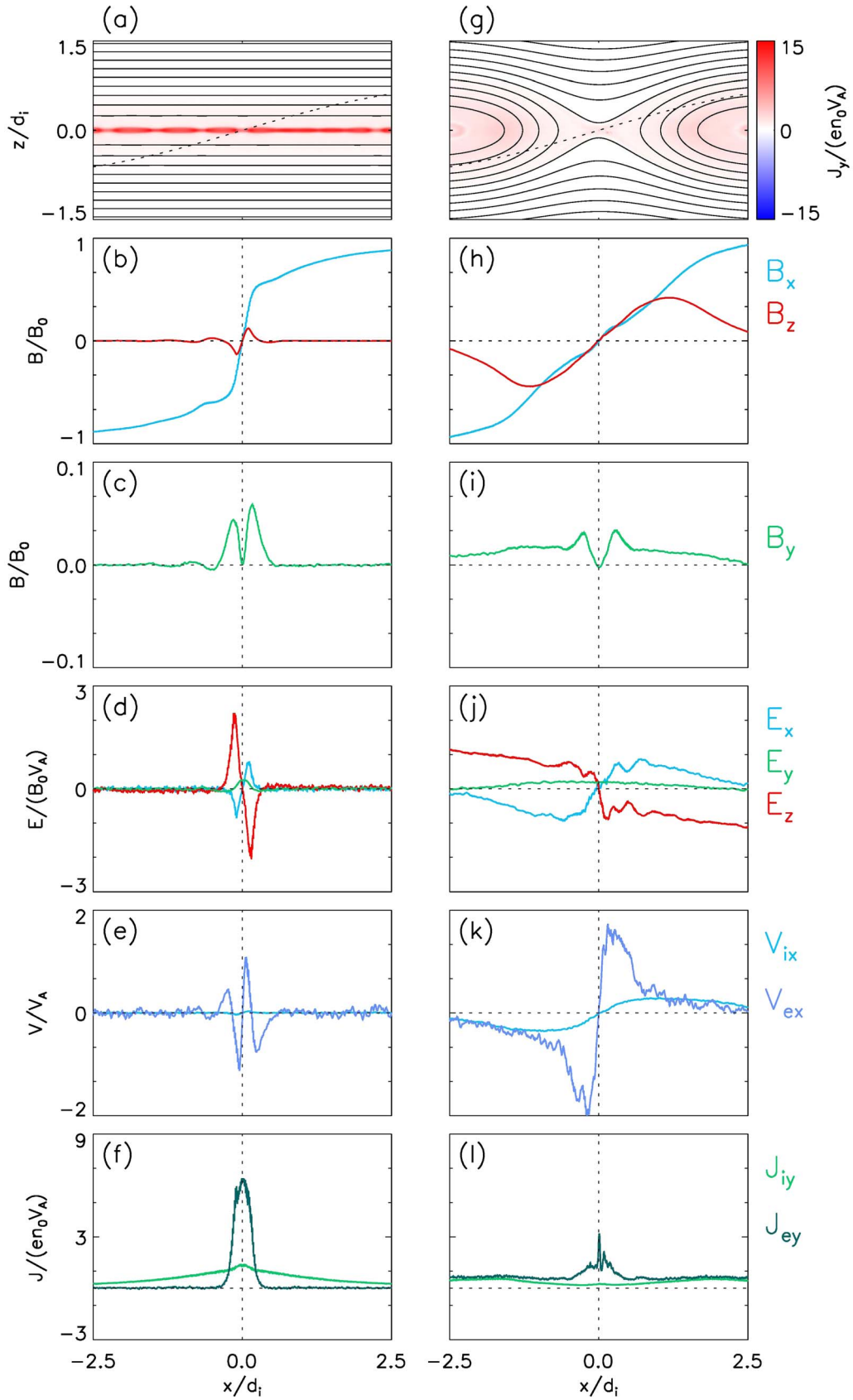


Figure 8. Current sheet J_y at $t =$ (a) $0.24\Omega_i^{-1}$, and (g) $5.07\Omega_i^{-1}$. The profiles along the black dashed line in (a) are on the left. The profiles along the black dashed line in (g) are on the right. (b) and (h): B_x , B_z . (c) and (i): B_y . (d) and (j): E_x , E_y , E_z . (e) and (k): V_{ix} , V_{ex} . (f) and (l): J_{iy} , J_{ey} .

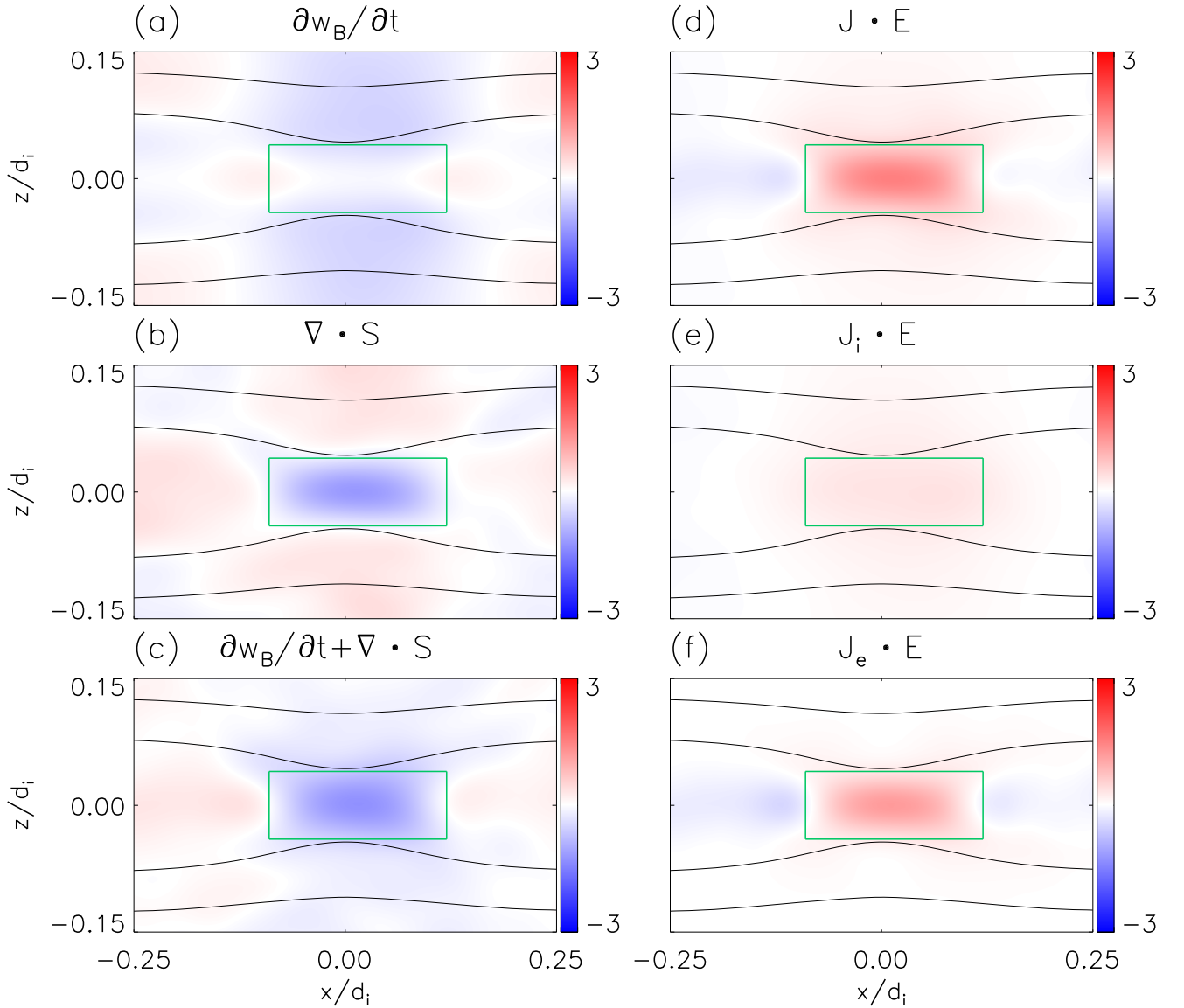


Figure 9. Calculations relating to the magnetic energy conversion equation at $t = 0.24\Omega_i^{-1}$. (a) Change rate of magnetic energy density $\frac{\partial w_B}{\partial t}$. (b) Divergence of the Poynting flux $\nabla \cdot \mathbf{S}$. (c) $\frac{\partial w_B}{\partial t} + \nabla \cdot \mathbf{S}$. (d) Work done by the electric field $\mathbf{J} \cdot \mathbf{E}$. (e) Work done to ions by electric field $\mathbf{J}_i \cdot \mathbf{E}$. (f) Work done to electrons by electric field $\mathbf{J}_e \cdot \mathbf{E}$. The region where $\mathbf{J} \cdot \mathbf{E}$ is strong is delineated by the green box.

Hall electric field to being coupled in reconnection by the Lorentz force.

Besides, the characteristic signals of reconnection, i.e., the Hall electric field and the Hall quadrupole magnetic field, are both at the sub-ion scale in the electron-only reconnection stage. With the transition to the standard reconnection stage, the signals above expand to the ion scale. Previous observation shows that in the electron-only reconnection event, the Hall electric field is confined to the electron current layer, while in the standard reconnection event, the Hall electric field is much wider than the electron current layer (Wang et al. 2020). The simulation in this work is consistent with the observation.

Furthermore, in magnetic reconnection, the distribution of converted magnetic energy between electrons and ions has been of great interest. In the electron-only reconnection stage in this paper, the magnetic energy conversion is mainly in the form of the Poynting flux flows (Figure 9(b)), which is

consistent with that in standard reconnection (Y. Shu et al. 2021). Our analysis further shows that, in electron-only reconnection, about two-thirds of the magnetic energy goes to electrons and one-third to ions. This is consistent with a recent statistical observation survey showing that electrons gain more internal energy than ions (S. Roy et al. 2024). However, in standard reconnection, more of the converted magnetic energy is transferred to the ions (M. Yamada et al. 2014; Y. Shu et al. 2021). For the outflows formed in electron-only reconnection, although the ion outflow speed is 2 orders of magnitude lower than the electron outflow speed, due to the real mass ratio $m_i/m_e = 1836$, the ion kinetic energy is still comparable to electron kinetic energy. However, the kinetic energy gained by ions is still less than the electron kinetic energy. This is consistent with the fact that ions are mainly accelerated by the Hall electric field in the electron-only reconnection stage, and the Hall electric field acts as an intermedia, converting the electron kinetic energy toward ion

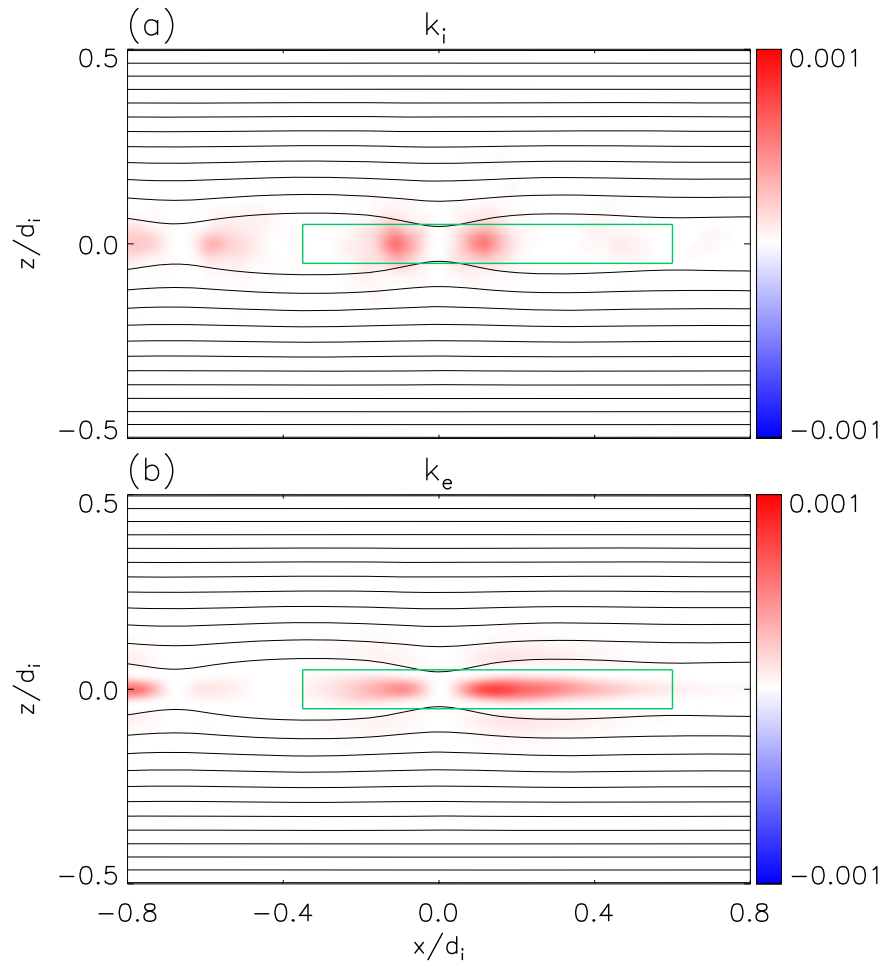


Figure 10. (a) The ion kinetic energy density $k_i = (1/2)n_i m_i V_{ix}^2$ and (b) the electron kinetic energy density $k_e = (1/2)n_e m_e V_{ex}^2$ at $t = 0.24\Omega_i^{-1}$. The outflow region is delineated by the green box.

kinetic energy (see Supporting Information in Y. Guan et al. 2024).

Thin electron-dominated current sheets in space plasma are usually formed under external drivers, and previous work demonstrated that driven reconnection in the sufficiently large domain first triggers electron-only reconnection and then evolves into standard reconnection (S. Lu et al. 2022). Simulation in this work excludes the effect of external drivers, suggesting that reconnection has to go through the electron-only reconnection stage before entering the standard reconnection stage. Besides, the electron-only reconnection stage in this simulation shows a fast reconnection rate, higher than the standard reconnection stage, while the reconnection rate of electron-only reconnection in S. Lu et al. (2022) is slow. The external driver has a significant impact on the buildup of the current sheet, and differences in the speed of the compression caused by external drivers can also have an effect. The process of the external driver compressing the current sheet deserves further study.





On the other hand, comparison with Y. Guan et al. (2024) shows that as long as electron-only reconnection emerges, keeping other parameters unchanged, only varying the length of the current sheets does not affect the electron outflow velocity and reconnection rate in electron-only reconnection. The mechanisms adjusting characteristics (e.g., reconnection rate and electron outflow speed) of electron-only reconnection should lie in the other parameters of the current sheets (e.g.,

plasma beta and current sheet thickness). Furthermore, considering electron-only reconnection often triggers under strong external drivers or in turbulent plasmas, complex background fluctuations in flows and electromagnetic fields may affect electron-only reconnection, which requires future investigation.

Acknowledgments

This research was funded by the Strategic Priority Research Program of the Chinese Academy of Sciences (grant Nos. XDB0560000 and XDB 41000000), the NSFC (grant Nos. 42230201 and 42274196), and the National Key Research and Development Program of China (grant No. 2022YFA1604600).

ORCID iDs

Yundan Guan  <https://orcid.org/0009-0000-3339-8818>
 Quanming Lu  <https://orcid.org/0000-0003-3041-2682>
 San Lu  <https://orcid.org/0000-0003-2248-5072>
 Rongsheng Wang  <https://orcid.org/0000-0002-9511-7660>

References

Angelopoulos, V., McFadden, J. P., Larson, D., et al. 2008, *Sci*, 321, 931
 Artemyev, A. V., Baumjohann, W., Petrukovich, A. A., et al. 2011, *AnGeo*, 29, 2253

- Artemyev, A. V., Petrukovich, A. A., Zelenyi, L. M., et al. 2009, *AnGeo*, **27**, 2075
- Asano, Y., Mukai, T., Hoshino, M., et al. 2003, *JGRA*, **108**, 1189
- Bessho, N., Chen, L., Stawarz, J. E., et al. 2022, *PhPI*, **29**, 042304
- Birn, J., Drake, J. F., Shay, M. A., et al. 2001, *JGRA*, **106**, 3715
- Birn, J., & Hesse, M. 2001, *JGRA*, **106**, 3737
- Birn, J., & Priest, E. R. 2007, *Reconnection of Magnetic Fields: Magnetohydrodynamics and Collisionless Theory and Observations* (Cambridge: Cambridge Univ. Press)
- Biskamp, D. 2000, *Magnetic Reconnection in Plasmas* (Cambridge: Cambridge Univ. Press)
- Borg, A. L., Øieroset, M., Phan, T. D., et al. 2005, *GeoRL*, **32**, L19105
- Burch, J. L., Torbert, R. B., Phan, T. D., et al. 2016, *Sci*, **352**, 1189
- Califano, F., Cerri, S. S., Faganello, M., et al. 2020, *FrP*, **8**, 317
- Chang, C., Huang, K., Lu, Q., et al. 2021, *JGRA*, **126**, e29290
- Fu, X. R., Lu, Q. M., & Wang, S. 2006, *PhPI*, **13**, 012309
- Gingell, I., Schwartz, S. J., Eastwood, J. P., et al. 2020, *JGRA*, **125**, e2019JA027119
- Guan, Y., Lu, Q., Lu, S., et al. 2023, *ApJ*, **958**, 172
- Guan, Y., Lu, Q., Lu, S., et al. 2024, *GeoRL*, **51**, e2024GL110787
- Goldman, M. V., Newman, D. L., & Lapenta, G. 2016, *SSRv*, **199**, 651
- Hesse, M., & Cassak, P. A. 2020, *JGRA*, **125**, 025935
- Hou, C., He, J., Duan, D., et al. 2024, *NatAs*, **8**, 1246
- Huang, C., Lu, Q., & Wang, S. 2010, *PhPI*, **17**, 072306
- Huang, C., Lu, Q., Guo, F., et al. 2015, *GeoRL*, **42**, 7282
- Huang, S., Xiong, Q., Song, L., et al. 2021, *ApJ*, **922**, 54
- Hubbert, M., Qi, Y., Russell, C. T., et al. 2021, *GeoRL*, **48**, e2020GL091364
- Hubbert, M., Russell, C. T., Qi, Y., et al. 2022, *JGRA*, **127**, e2021JA029584
- Ji, H., Daughton, W., Jara-Almonte, J., et al. 2022, *NatRP*, **4**, 263
- Karimabadi, H., Daughton, W., & Scudder, J. 2007, *GeoRL*, **34**, L13104
- Lin, J., & Forbes, T. G. 2000, *JGR*, **105**, 2375
- Lu, Q. M., Fu, H., Wang, R., & Lu, S. 2022, *ChPhB*, **31**, 089401
- Lu, Q. M., Guo, A., Yang, Z., et al. 2024, *ApJ*, **964**, 33
- Lu, Q. M., Huang, C., Xie, J., et al. 2010, *JGRA*, **115**, A11208
- Lu, Q. M., Yang, Z., Wang, H., et al. 2021, *ApJ*, **919**, 28
- Lu, S., Angelopoulos, V., Artemyev, A. V., et al. 2020a, *PhPI*, **27**, 102902
- Lu, S., Angelopoulos, V., Pritchett, P. L., et al. 2021, *JGRA*, **126**, e29550
- Lu, S., Artemyev, A. V., Angelopoulos, V., et al. 2019, *JGRA*, **124**, 1052
- Lu, S., Lu, Q. M., Cao, Y., et al. 2011, *ChSBu*, **56**, 48
- Lu, S., Lu, Q. M., Wang, R. S., et al. 2022, *GeoRL*, **49**, e2022GL098547
- Lu, S., Wang, R. S., Lu, Q. M., et al. 2020b, *NatCo*, **11**, 5049
- Man, H. Y., Zhou, M., Yi, Y. Y., et al. 2020, *GeoRL*, **47**, e2020GL089659
- Masuda, S., Kosugi, T., Hara, H., et al. 1994, *Natur*, **371**, 495
- Nagai, T., Shinohara, I., Fujimoto, M., et al. 2001, *JGR*, **106**, 25929
- Nagai, T., Shinohara, I., Fujimoto, M., et al. 2003, *JGR*, **108**, 1357
- Nelson, C. J., Shelyag, S., Mathioudakis, M., et al. 2013, *ApJ*, **779**, 125
- Ng, J., Chen, L., Bessho, N., et al. 2022, *GeoRL*, **49**, e2022GL099544
- Phan, T. D., Eastwood, J. P., Shay, M. A., et al. 2018, *Natur*, **557**, 202
- Phan, T. D., Gosling, J. T., Davis, M. S., et al. 2006, *Natur*, **439**, 175
- Pritchett, P. L. 2001, *JGRA*, **106**, 3783
- Pritchett, P. L., & Coroniti, F. V. 1994, *GeoRL*, **21**, 1587
- Pyakurel, P. S., Shay, M. A., Phan, T. D., et al. 2019, *PhPI*, **26**, 082307
- Roy, S., Bandyopadhyay, R., Matthaeus, W. H., & Pyakurel, P. S. 2024, *ApJ*, **964**, 44
- Sang, L., Lu, Q. M., Xie, J. L., et al. 2022, *PhPI*, **29**, 102108
- Shay, M. A., Drake, J. F., Rogers, B. N., et al. 2001, *JGRA*, **106**, 3759
- Shay, M. A., Drake, J. F., & Swisdak, M. 2007, *PhRvL*, **99**, 155002
- Shen, C., Chen, B., Reeves, K. K., et al. 2022, *NatAs*, **6**, 317
- Shi, P. Y., Srivastav, P., Barbhuiya, M. H., et al. 2022a, *PhRvL*, **128**, 025002
- Shi, P. Y., Srivastav, P., Barbhuiya, M. H., et al. 2022b, *PhPI*, **29**, 032101
- Shu, Y., Lu, S., Lu, Q., Ding, W., & Wang, S. 2021, *JGRA*, **126**, e2021JA029712
- Stawarz, J. E., Eastwood, J. P., Phan, T. D., et al. 2019, *ApJL*, **877**, L37
- Stawarz, J. E., Eastwood, J. P., Phan, T. D., et al. 2022, *PhPI*, **29**, 012302
- Torbert, R. B., Burch, J. L., Phan, T. D., et al. 2018, *Sci*, **362**, 1391
- Vega, C., Roytershteyn, V., Delzanno, G. L., & Boldyrev, S. 2020, *ApJL*, **893**, L10
- Vörös, Z., Varsani, A., Yordanova, E., et al. 2021, *JGRA*, **126**, e2021JA029415
- Wang, R. S., Lu, Q. M., Nakamura, R., et al. 2018, *GeoRL*, **45**, 4542
- Wang, R. S., Lu, Q. M., Lu, S., et al. 2020, *GeoRL*, **47**, e2020GL088761
- Wang, R. S., Wang, S., Lu, Q., et al. 2023, *NatAs*, **7**, 18
- Wang, S., & Lu, Q. M. 2019, *Collisionless Magnetic Reconnection* (Beijing: Science Press)
- Wang, S. M., Lu, S., Lu, Q., et al. 2024, *SciA*, **10**, eado4639
- Wygant, J. R., Cattell, C. A., Lysak, R., et al. 2005, *JGRA*, **110**, A09206
- Yamada, M., Kulsrud, R., & Ji, H. 2010, *RvMP*, **82**, 603
- Yamada, M., Yoo, J., Jara-Almonte, J., et al. 2014, *NatCo*, **5**, 4774
- Zhang, T. L., Lu, Q. M., Baumjohann, W., et al. 2012, *Sci*, **336**, 567
- Zhang, Z., Lu, S., Lu, Q., et al. 2024, *JGRA*, **129**, e2024JA032575
- Zhuo, R., He, J., Duan, D., Zhu, X., & Hou, C. 2024, *ApJ*, **969**, 47